J. Fluid Mech. (2011), *vol.* 679, *pp.* 476–504.
doi:10.1017/jfm.2011.142

The $Pe \sim 1$ regime of convection across a horizontal permeable membrane

G. V. RAMA REDDY[1]† AND BABURAJ A. PUTHENVEETTIL[2]

[1]Heat Transfer and Fluid Flow, Corporate R&D, Bharat Heavy Electricals Ltd., Hyderabad 500093, India

[2]Department of Applied Mechanics, Indian Institute of Technology Madras, Chennai 600036, India

(Received 16 August 2010; revised 16 February 2011; accepted 17 March 2011; first published online 17 May 2011)

In natural convection, driven by an unstable density difference due to a heavier fluid (brine) above a lighter fluid (water) across a horizontal permeable membrane, we discover a new regime of convection, where the Sherwood number (Sh) scales approximately as the Rayleigh number (Ra). Inferring from the planforms of plume structure on the membrane and the estimates of velocity through the membrane, we show that such a regime occurs when advection balances diffusion in the membrane, i.e. the Péclet number based on the membrane thickness (Pe) is of order one. The advection is inferred to be caused by the impingement of the large-scale flow on the membrane. Utilizing mass balance and symmetry assumptions in the top and the bottom fluids, we derive an expression for the concentration profile in the membrane pore in the new regime by solving the convection–diffusion equation in the membrane pore; this helps us to obtain the concentration drops above and below the membrane that drive the convection. We find that the net flux, normalised by the diffusive flux corresponding to the concentration drop on the side opposite to the impingement of the large-scale flow remains constant throughout the new regime. On the basis of this finding, we then obtain an expression for the flux scaling in the new regime which matches with the experiments; the expression has the correct asymptotes of flux scaling in the advection and the diffusion regimes. The plume spacings in the new regime are distributed lognormally, and their mean follows the trend in the advection regime.

Key words: buoyancy-driven instability, plumes/thermals, turbulent convection

1. Introduction

When a horizontal permeable membrane separates a heavier miscible fluid above it from a lighter fluid below, based on the unstable density difference across the membrane that keeps decreasing with time, various regimes of convection are set up. At large concentration differences, the transport across the membrane will be due to advection (Puthenveettil & Arakeri 2008) while diffusion across the membrane will be predominant at lower concentration differences (Puthenveettil & Arakeri 2005). The present study investigates the phenomena that occur when advection balances diffusion in such a membrane. In all the cases, unstable layers of fluid above and below the membrane cause turbulent convection away from the membrane; the

† Email address for correspondence: gvramareddy@gmail.com

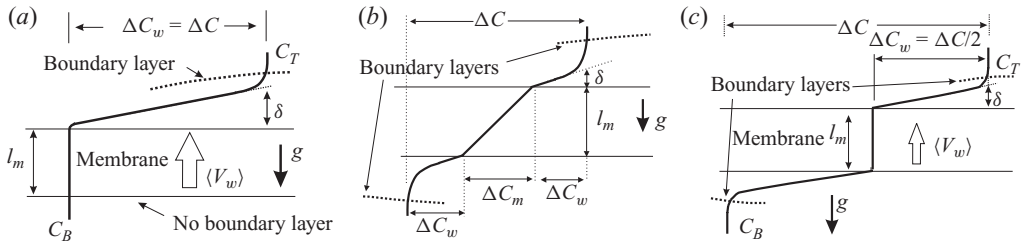

FIGURE 1. Inferred concentration profiles across the membrane pore in the experiments by PA. (*a*) The advection regime, (*b*) the diffusion regime and (*c*) the combined regime.

arrangement could thus be used to study the effect of wall-normal advection or diffusion on turbulent convection. In addition to the importance of understanding the phenomenology of such a system, the effects encountered in such a configuration are of considerable practical interest in systems where unstable concentration boundary layers affect the transport across membranes (Slezak, Dworecki & Anderson 1985; Dworecki *et al.* 2005; Slezak *et al.* 2010).

The presence of an advection and a diffusion regime in convection across a permeable membrane was demonstrated by Puthenveettil & Arakeri (2008, hereafter referred to as PA) using brine solution above water, separated by a membrane of pore size 35 μm, thickness, $l_m = 70\,\mu\text{m}$ and open area factor, $\Gamma = 0.25$. The dimensionless parameters that characterise convection in such a case are the Rayleigh number, $Ra = g\beta\Delta C H^3/(\nu D)$, the Schmidt number ($Sc = \nu/D$) and the aspect ratio, $\zeta = L/H$. Here, g is the acceleration due to gravity, β is the coefficient of salinity, ΔC is the concentration difference between the bulk fluids on both sides of the membrane, H is height of the fluid layer above/below the membrane, ν is the kinematic viscosity, D is the species diffusivity and L is the horizontal dimension of the fluid layer. For $Ra > 3.5 \times 10^{11}$, PA found that advection across the membrane, generated by a continuous overturning of the unstable system itself, dominated the transport across the membrane, with no concentration drop across the membrane (figure 1*a*). In such a situation, the dimensionless membrane parameter $\varkappa = \kappa^2/l_m^4$ determines the membrane resistance to flow through it, where κ is the membrane permeability. In addition, the D'Arcy–Rayleigh number of the membrane $Ra_\kappa = g\beta\Delta C\kappa l_m/\nu D$ gives the relative strength of buoyancy and dissipative effects in the membrane. In such an advection regime of convection across the membrane, the dimensionless mass flux, given by the Sherwood number $Sh = q/(D\Delta C/H)$, where q is the mass flux of the solute, depends on all the above dimensionless parameters as

$$Sh = C_2 \varkappa Ra_\kappa Gr = \varkappa_1 \frac{Ra^2}{Sc}, \tag{1.1}$$

where C_2 is a prefactor and $\varkappa_1 = C_2\varkappa\kappa l_m/H^3$.

At lower concentration differences, i.e. at $Ra < 7 \times 10^{10}$, PA inferred that pure diffusion occurs through the membrane, resulting in a linear concentration drop across the membrane (figure 1*b*). The situation was analogous to convection from a plate with appreciable temperature drop across the plate, and Sh is then only a function of Rayleigh number based on the concentration drop above/below the membrane (Puthenveettil & Arakeri 2005). The flux scaled as $Sh \sim Ra_w^{1/3}$, similar to that in turbulent convection over horizontal surfaces, when the effective Rayleigh

number

$$Ra_w = \frac{g\beta\Delta C_w H^3}{\nu D} \tag{1.2}$$

was defined based on the concentration drop ΔC_w above or below the membrane (figure 1*b*). This implies that the mass transport above and below the membrane becomes similar to heat transport in turbulent natural convection above flat horizontal surfaces. A similar diffusion regime was also observed by Puthenveettil & Arakeri (2005, hereafter referred to as PA05) at a higher Ra_w ($0.5\text{–}2 \times 10^{11}$) by using a membrane with a much smaller pore size (0.45 μm).

At ΔC in between these two regimes, PA observed a regime, which they termed as the combined regime, with an inferred concentration profile as shown in figure 1(*c*), where $Sh \sim Ra_w^{1/3}$ with $\Delta C_w = \Delta C/2$. They proposed that suction due to detaching plumes on both sides of the membrane causes negligible concentration drop across the membrane in this regime. The boundary layers could then retain their nature as natural convection boundary layers, to give the above flux scaling. However, this phenomenology is still unverified and the transition between the limiting cases of pure advection across the membrane (PA) and pure diffusion across the membrane (PA05; PA) is not well understood. For example, it is intriguing that the advection-dominated concentration profile of figure 1(*a*) would change over to that of the diffusion-dominated profile (figure 1*b*) without having a regime where advection balances diffusion in the membrane. It is not known whether the transition scenario observed by PA is the general case or whether it is an exception unique to the membrane used by them. Understanding these and similar issues about the transition range between advection and diffusion is necessary to gain a better knowledge of the phenomena that occur in convection across membranes. The present study explores the intermediate range between the two limits of advection and diffusion and finds that there is a range of Ra in which the flux scales differently from that in all the other regimes.

We study convection in an arrangement similar to PA, with a layer of brine above a layer of water, across a horizontal permeable membrane to achieve high Ra ($\sim 10^{11}$) and high Sc (~ 600), but with the membrane being coarser (45.6 μm) and thicker (72.5 μm) than that used in PA. Since the membrane pore size is 10^5 times the ionic diameters of Na^+ (1.98 Å) and Cl^- (3.62 Å), the membrane is not selective and the diffusion coefficients of NaCl are the same in the membrane and the bulk. The use of such a membrane results in the initial advection velocities through the membrane being about $0.004\,\mathrm{cm\,s^{-1}}$, half of that in PA at the same starting concentration difference. The velocity through the membrane is an order smaller than the velocity in the bulk ($\sim 0.3\,\mathrm{cm\,s^{-1}}$). In such a situation, the range of Ra over which the transition from advection to diffusion occurs inside the membrane is extended. We find a new regime of flux scaling in this transition Ra range, which we show occurs when advection balances diffusion inside the membrane. Unstable liquid layers giving rise to sheet plumes are formed on the membrane surface, the structure of which we use to infer the nature of the new regime. Since the relevant parameter that determines the relative magnitude of advection and diffusion inside the membrane pore is the membrane Péclet number,

$$Pe = \frac{\langle V_w \rangle l_m}{D}, \tag{1.3}$$

where $\langle V_w \rangle$ is the mean velocity through the membrane pore, the new regime occurs when $Pe \sim 1$.

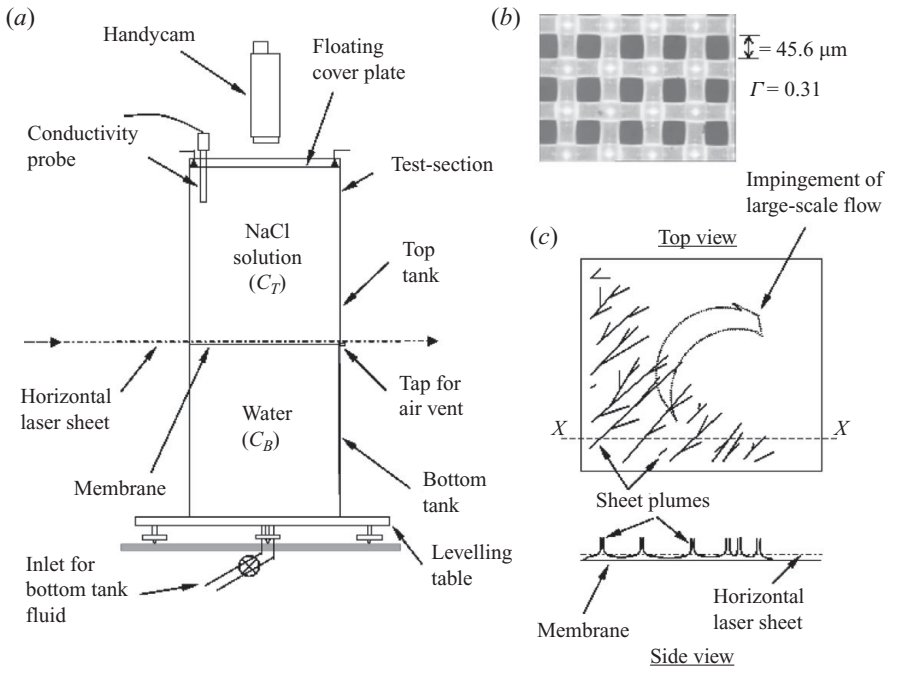

FIGURE 2. (*a*) Schematic diagram of the experimental set-up, (*b*) magnified (100×) view of the permeable membrane used in the present experiments and (*c*) methodology of visualisation showing the side view of the sheet plumes in the vertical plane X–X in the top view, due to an intersecting horizontal laser sheet, along with the associated planform.

This paper is organised as follows. Using the experimental arrangement described in § 2, we find the flux and the planform plume structure evolution with Ra_w in a typical experiment in § 3. We first show in § 3 that the scaling of flux obtained in the new regime is approximately $Sh \sim Ra$, quite different from that in the two limiting cases of the advection and diffusion regimes. Drawing inferences from the planform plume structure, we show in § 4 that the new regime occurs when the Péclet number based on the membrane thickness is of order one. The remaining part of the paper focuses on this new regime. In § 4.1, we derive the concentration profile in the membrane in the regime, from which we obtain the concentration drop across the membrane. This helps us to obtain the relevant driving potential for convection above and below the membrane. We find that the signature of the new regime is that the net flux, when normalised by this relevant driving potential remains a constant in the new regime. Starting from this finding, we then obtain a flux scaling expression valid in the new regime, which has the correct limits in the advection and diffusion regimes. We also draw inferences about the boundary layers in the new regime based on the plume spacing measurements in § 4.2.

2. Experimental set-up and measurements

2.1. *Set-up and procedure*

A schematic diagram of the experimental set-up is shown in figure 2(*a*). Since the set-up is similar to that in PA, with the difference that the membrane used in the present study is coarser and thicker, we briefly summarise the relevant details of

the set-up; the reader is referred to Rama Reddy (2009) and PA for further details. A membrane ($\Gamma = 0.31$, pore size $P_s = 45.6\,\mu\text{m}$ and thickness $l_m = 72.5\,\mu\text{m}$) is stretched tightly and fixed horizontally between a top and a bottom glass tank of inner cross-section 15 cm $\times$ 15 cm. The zoomed view of the membrane is shown in figure 2(*b*). The bottom tank is filled with distilled water having 0.96 p.p.m. of rhodamine-6G up to the level of the membrane. Sodium chloride solution, prepared to the desired initial concentration C_T^0, is then filled in the top tank so that the height of the fluid layer in each tank is $H = 23.6\,\text{cm}$. In the present study, we use starting concentrations of $C_T^0 = 10\,\text{g}\,\text{l}^{-1}$, $8\,\text{g}\,\text{l}^{-1}$ and $6\,\text{g}\,\text{l}^{-1}$. The upper surface of the membrane is covered with a Perspex sheet to avoid initial mixing while filling. The Perspex sheet is removed to start the experiment, and a typical experiment runs approximately for 2.5 days, by which time density equalisation occurs between the two tanks. An acrylic plate is kept floating on the free surface of the salt solution to prevent evaporation and maintain the same boundary conditions in both the tanks.

2.2. *Diagnostics and measurements*

The sheet plumes above the membrane become visible due to the laser-induced fluorescence of the lighter fluid in the plumes which intersects a horizontal laser sheet grazing the membrane above it. A pulsed Nd:Yag laser (Litron, 532 nm, 100 mJ pulse^{-1} and 50 Hz.) is used to obtain a diverging horizontal light sheet by passing the laser beam through a sheet-optics arrangement. The vertical position of the laser sheet is adjusted to <1 mm above the membrane when visualising the planform of the near-membrane plumes by a handycam (SONY® DCR-DVD 708E). Figure 2(*c*) shows the schematic diagram of the visualisation method along with the side view in the X–X plane. A good fluorescence intensity is observed when the initial concentration of the dye in the bottom tank solution is 0.96 p.p.m. Since the dimensionless density difference $(\Delta\rho/\rho)_{dye} \ll (\Delta\rho/\rho)_{salt}$, and $Sc_{dye} \gg Sc_{salt}(2000 \gg 600)$, the dye acts as a passive scalar, following the convection and diffusion patterns of the salt solution.

The concentration of salt in the top tank solution $C_T(t)$, which changes with time t, is estimated from transient measurements of the electrical conductivity of the top tank solution, by a four-pole conductivity probe (Radiometer Analytical SAS 2006). The probe was immersed to a depth of 5.5 cm from the top tank liquid layer height. The least count of the probe is $0.001\,\mu\text{S}\,\text{cm}^{-1}$ and the accuracy is $\pm 2\,\%$ of reading; the precision of the probe is approximately $0.005\,\text{g}\,\text{l}^{-1}$. The conductivity readings are corrected to a reference temperature of 25°C using the temperature correction factor for sodium chloride solution of 2.12 % °C^{-1}. Since there is a finite volume of about 3.8 cc between the electrodes that are spaced by 0.5 cm, the conductivity probe measures a local spatial average of the electrical conductivity of the solution. Even though the measuring current is passed at a high frequency of about 2000 Hz, the probe averages the data over time electronically and acquires at a rate of 1 reading in 0.64 s. The effect of rhodamine-6G on the measured conductivity of the salt solution is negligible due to the low concentration of dye used (Rama Reddy 2009). The handycam and the conductivity meter are synchronised so that the Rayleigh number for any planform of plume structures can be calculated from the conductivity data.

2.3. *Calculation of flux and the concentration difference*

We assume that the temporally and locally spatially averaged concentration C_T that the probe measures represents the concentration of the entire top tank. This assumption is generally true for turbulent convection with thin boundary layers and well-mixed bulk. It is shown in Appendix A that the expected error due to the well-mixed

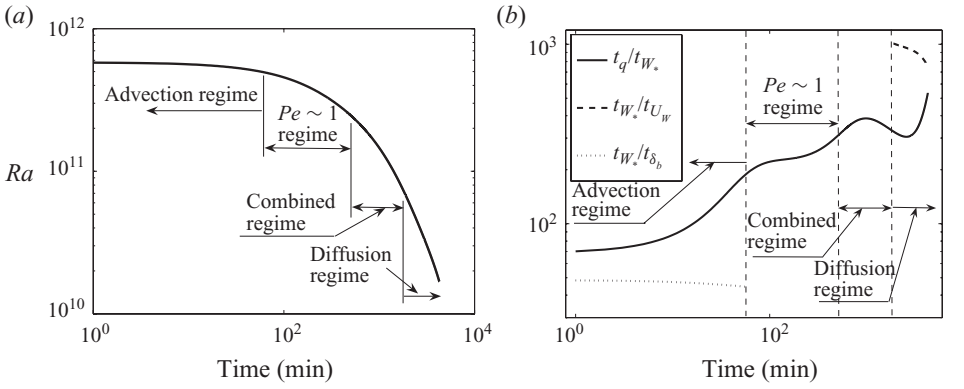

FIGURE 3. (*a*) Variation of the Rayleigh number with time in a $C_T^0 = 10\,\mathrm{g\,l^{-1}}$ experiment. (*b*) Variation of the ratio of time scales with time in a $C_T^0 = 10\mathrm{g\,l^{-1}}$ experiment.

assumption is negligible. Appendix B shows that the bulk in the present study is fully turbulent. Here C_T is calculated from the measured conductivity of the top tank solution, using the standard relation between conductivity and concentration for NaCl solution (Lide 2003). Using mass conservation, the concentration difference between the tanks at any instant is

$$\Delta C(t) = C_T(t) - C_B(t) = 2C_T(t) - C_T^0, \tag{2.1}$$

where $C_B(t)$ is concentration in the bottom tank. The Rayleigh numbers can now be calculated from ΔC; figure 3(*a*) shows the variation of Ra with time in an experiment with $C_T^0 = 10\,\mathrm{g\,l^{-1}}$. From the conservation of mass in the top tank, the flux of salt across the membrane is

$$q = -H\frac{\mathrm{d}C_T}{\mathrm{d}t}. \tag{2.2}$$

Note that this is an area-averaged, uniform flux over the membrane surface. Differentiation of the raw concentration data with time to calculate q from (2.2) results in large fluctuations. We hence use an exponential decay curve of the form

$$C_T = A_0 + A_1\,\mathrm{e}^{-t/d_1} + A_2\,\mathrm{e}^{-t/d_2} + A_3\,\mathrm{e}^{-t/d_3} + A_4\,\mathrm{e}^{-t/d_4}, \tag{2.3}$$

where A_0 to A_4 and d_1 to d_4 are fit coefficients, fitted through the C_T versus t data to calculate the derivatives. The reasons for choosing a fit of the form (2.3) are given in Appendix C. A sum of four exponentials is used owing to the presence of four regimes of convection, as discussed in § 3.

2.4. *Quasi-steady assumption*

The phenomena in the bulk could be considered quasi-steady if the time of one large-scale circulation $t_{W_*} = H/W_* \ll$ the time scale of decrease of flux $t_q = q/(\mathrm{d}q/\mathrm{d}t) = (\mathrm{d}C_T/\mathrm{d}t)/(\mathrm{d}^2C_T/\mathrm{d}t^2)$. Here

$$W_* = (g\beta q H)^{1/3} \tag{2.4}$$

is the Deardorff velocity scale (Deardorff 1970), which is proportional to the velocity of the large-scale circulation (PA05). When we refer to the large-scale circulation here, we mean the coherent circulation that is set up in the top tank, which results in a mean shear near the membrane. Our observations show that within a few seconds of the removal of the Perspex sheet covering the membrane, a large-scale circulation is set up. Note that t_q varies from 60.7 min at the beginning of the experiment to

2797.2 min at the end; t_{W*} varies from 0.89 to 5.22 min from the beginning to the end of the experiment. Figure 3(b) shows the variation of t_q/t_{W*} with time. Even at the start of the experiment, where the flux changes at its fastest rate, $t_q/t_{W*} \gg 1$, implying that many large-scale circulations will observe a constant flux.

The phenomena near the membrane would be quasi-steady if their time scales are much smaller than the time of one large-scale circulation. A possible length scale near the membrane in the diffusion regime, obtained from dimensional arguments by Theerthan & Arakeri (1998), is

$$Z_w = (\nu D/g\beta\Delta C_w)^{1/3}, \tag{2.5}$$

where Z_w is proportional to the critical boundary layer thickness ($\delta_c \sim 10Z_w$; Theerthan & Arakeri 1994) and to the mean plume spacing ($\lambda_m \sim 92Z_w$ for $Sc \sim 600$; Theerthan & Arakeri 1998, 2000; Puthenveettil & Arakeri 2005). The associated characteristic time scale for the near-membrane phenomena in the diffusion regime is

$$t_{U_w} \sim Z_w^2/\sqrt{\nu D}, \tag{2.6}$$

where t_{U_w} is proportional to the time of growth of the boundary layer and to the time of merging of sheet plumes. Figure 3(b) shows that $t_{W*}/t_{U_w} \gg 1$ in the diffusion regime for a typical experiment. Similarly, the time scale $t_{Wo} = D/W_o^2$ associated with the Townsend's velocity scale $W_o = (g\beta q D)^{1/4}$ near the membrane (Townsend 1959) is also smaller than t_{W*} (0.07 s $\leqslant t_{Wo} \leqslant$ 0.91 s). The above estimate is accurate only to a factor of $\sqrt{Sc}$, more rigorous estimates based on the assumption of laminar natural convection boundary layers between the sheet plumes are given in Appendix D. These estimates show that the ratio of large-scale flow time scale to the near-membrane time scale is around 10. Similar to these estimates, the observed mean merging time of two sheet plumes in the diffusion regime is of the order of 10 s while the time period of a large-scale flow circulation is of the order of 100 s. We could hence expect the boundary layer and the plumes in the diffusion regime to see a constant strength of large-scale flow over their lifespan.

A similar conclusion is obtained in the advection regime by estimating the time scales of the phenomena near the membrane. A possible near-wall time scale is $t_{\delta_b} = \delta_b/U_b$, where δ_b is the boundary layer thickness in the presence of advection, given by PA as

$$\delta_b \sim \left(\frac{\langle V_i\rangle \nu x^2}{g\beta\Delta C}\right)^{1/4}, \tag{2.7}$$

where $\langle V_i\rangle = \Gamma\langle V_w\rangle$ is the advection velocity just above/below the membrane. U_b is the horizontal velocity in such boundary layers, given by PA as

$$U_b \sim \left(\frac{\langle V_i\rangle^3 x^2 g\beta\Delta C}{\nu}\right)^{1/4}. \tag{2.8}$$

Using (2.7) and (2.8), t_{δ_b} can be expressed as,

$$t_{\delta_b} \sim \frac{Z_{V_i}}{V_{Z_i}}, \tag{2.9}$$

where $V_{Z_i} = \sqrt{g\beta\Delta C Z_{V_i}}$ is the free-fall velocity over the advection length scale $Z_{V_i} = \nu/\langle V_i\rangle$. Figure 3($b$) shows that $t_{W*}/t_{\delta_b} \gg 1$ in the advection regime; the strength of large-scale flow remains approximately same over the time period of growth of the boundary layer in the presence of advection across the membrane.

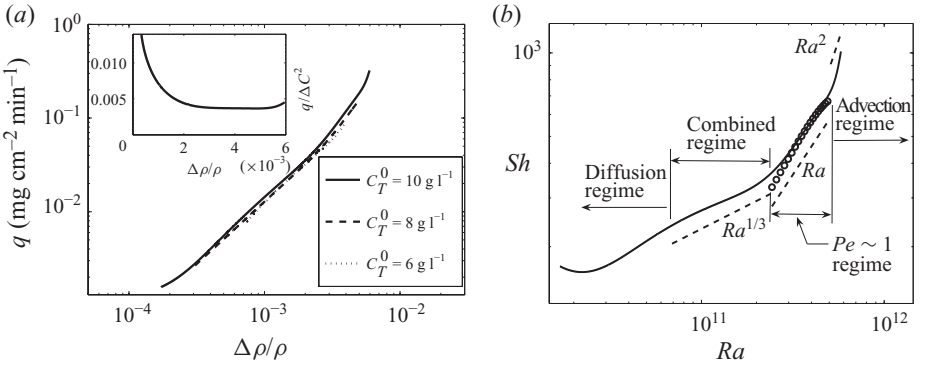

FIGURE 4. (*a*) Variation of the flux (2.2) with the dimensionless density difference $\Delta\rho/\rho$. The inset shows that $q \sim \Delta C^2$ for $2.5 \times 10^{-3} \leqslant \Delta\rho/\rho \leqslant 5.1 \times 10^{-3}$. (*b*) Variation of the Sherwood number with the Rayleigh number for the $C_T^0 = 10\,\mathrm{g\,l^{-1}}$ experiment in (*a*). The open circles are the theoretical prediction of (4.18).

In the regime where advection and diffusion are important, we expect the near-membrane time scales to be intermediate to those obtained in the diffusion and the advection regime. Since t_{W*}/t_{U_w} and t_{W*}/t_{δ_b} are both much greater than one, we expect the similar ratio in the new intermediate regime also to be greater than one. Further, the average time for the merging of near-membrane plumes in the intermediate regime was about 13 s, which is much smaller than the time of 81 s of one large-scale circulation at the same Ra. The quasi-steady approximation can hence be made in all the subsequent analysis. Hence, even though the flux changes with time, the large-scale flow and the near-membrane phenomena experience a constant flux over their lifetimes; the convection is quasi-steady. The present experimental results can hence be compared to steady convection systems such as Rayleigh–Bénard convection (RBC).

3. Identification of the regimes of convection

During the course of an experiment, mixing of the solutions in the two tanks occurs, ΔC and q decreases with time. However, since the system is quasi-steady, representation of the evolution of dependent variables (say flux) as a function of the independent variables (ΔC or Ra) – rather than as a function of time – in a single experiment is equivalent to a similar representation obtained from many steady-state experiments. Figure 4(*a*) shows the dependence of q on the dimensionless density difference $\Delta\rho/\rho\,(=\beta\Delta C)$ for typical experiments started with $C_T^0 = 10\,\mathrm{g\,l^{-1}}$, $8\,\mathrm{g\,l^{-1}}$ and $6\,\mathrm{g\,l^{-1}}$. Lower C_T^0 experiments were conducted to visualise the plume structure during the later part of the experiments, since mixing reduces the contrast of the plume structure in the planform images. The slope of the curve for the experiment with $C_T^0 = 10\,\mathrm{g\,l^{-1}}$ changes thrice at $\Delta\rho/\rho = 5.1 \times 10^{-3}$, 2.5×10^{-3} and 0.71×10^{-3}, indicating four different regimes of convection. The changes of the slope seen in figure 4(*a*) could be observed more clearly in the Sh versus Ra plot of figure 4(*b*), at $Ra = 4.96 \times 10^{11}$, 2.43×10^{11} and 0.69×10^{11}. For $Ra > 4.96 \times 10^{11}$, the dimensionless flux scales as $Sh \sim Ra^2$ or $q \sim \Delta C^3$, similar to that observed by PA in their advection regime. The planform of plume structure in this regime was also similar to that in the advection regime of PA (their figure 8*a*). The agreement of the present data with the Ra^2 scaling seems to be approximate as the range of this regime is less in the present

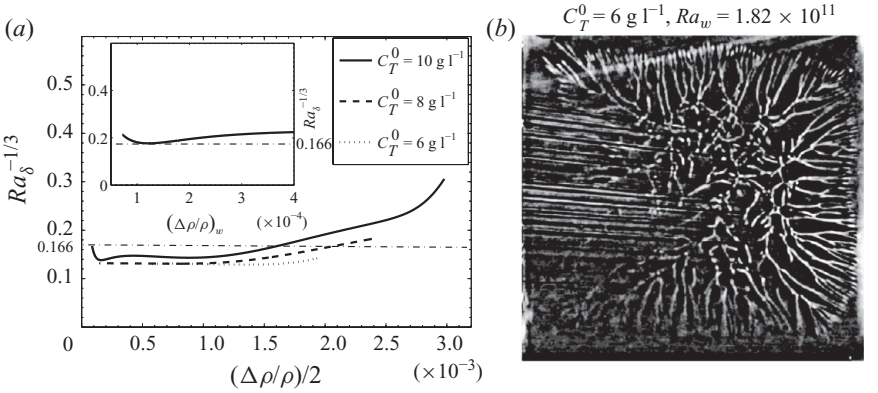

FIGURE 5. (*a*) Variation of $Ra_\delta^{-1/3}$ (3.1) with $(\Delta\rho/\rho)/2$, when $\Delta C_w = \Delta C/2$ for the flux data shown in figure 4(*a*). The inset shows the variation of $Ra_\delta^{-1/3}$, with $\Delta C_w = (\Delta C - \Delta C_m)/2$. (*b*) Planform of plume structure at the beginning of the combined regime. Table 1 shows the parameters corresponding to the image.

study. In any case, the focus of this paper is not on the advection regime, which has been explored thoroughly by PA.

Since differences in the near-membrane phenomena will be reflected strongly in the variation of the flux normalised by the near-membrane scales as

$$Ra_\delta^{-1/3} = \frac{q}{D\Delta C_w/Z_w}, \tag{3.1}$$

we study the variation of $Ra_\delta^{-1/3}$ below. Here, Ra_δ is the Rayleigh number based on $\delta = D\Delta C_w/q$, the diffusion layer thickness and ΔC_w. Here $\Delta C_w = \Delta C$ in the advection regime (figure 1*a*), $\Delta C_w = (\Delta C - \Delta C_m)/2$ in the diffusion regime (figure 1*b*) and $\Delta C_w = \Delta C/2$ in the combined regime (figure 1*c*). In all the subsequent analyses, the effective Rayleigh number, Ra_w, in any regime is based on the corresponding ΔC_w in that regime. Note that $Ra_\delta^{-1/3} = 0.166$ if the boundary layers above/below the membrane maintain their character the same as those in RBC (Theerthan & Arakeri 2000).

Figure 5(*a*) shows that for $3.5 \times 10^{-4} \leqslant \frac{1}{2}(\Delta\rho/\rho) \leqslant 1.25 \times 10^{-3}$, ($6.9 \times 10^{10} \leqslant Ra \leqslant 2.43 \times 10^{11}$ in figure 4*b*), $Ra_\delta^{-1/3}$ with $\Delta C_w = \Delta C/2$ is constant and is approximately equal to the value in RBC, similar to that in the combined regime in figure 7(*b*) of PA. In addition, as expected in the combined regime of PA, sheet plumes occupy the total area of the membrane in the planform in figure 5(*b*) at $\Delta\rho/\rho = 3.6 \times 10^{-3}$ in this regime. The white lines in the image are the top view of the sheets of lighter fluid rising from the membrane surface. The concentration profile in this regime could hence be expected to be as in figure 1(*c*). At even lower Ra, $Ra < 6.9 \times 10^{10}$ in figure 4(*b*) or $(\Delta\rho/\rho)_w < 2.7 \times 10^{-4}$, in the inset in figure 5(*a*), $Ra_\delta^{-1/3}$ defined using $\Delta C_w = (\Delta C - \Delta C_m)/2$, is approximately equal to that in RBC, proving the presence of a diffusion regime; the concentration profile in this regime could be inferred to be as shown in figure 1(*b*). The transport of salt through the membrane in this regime is entirely due to diffusion and the boundary layers in this regime are similar to those in RBC (PA05; PA). The regimes below $Ra = 2.43 \times 10^{11}$ are hence the same as those observed by PA. We do not discuss these combined and diffusion regimes further as they have been discussed in detail by PA.

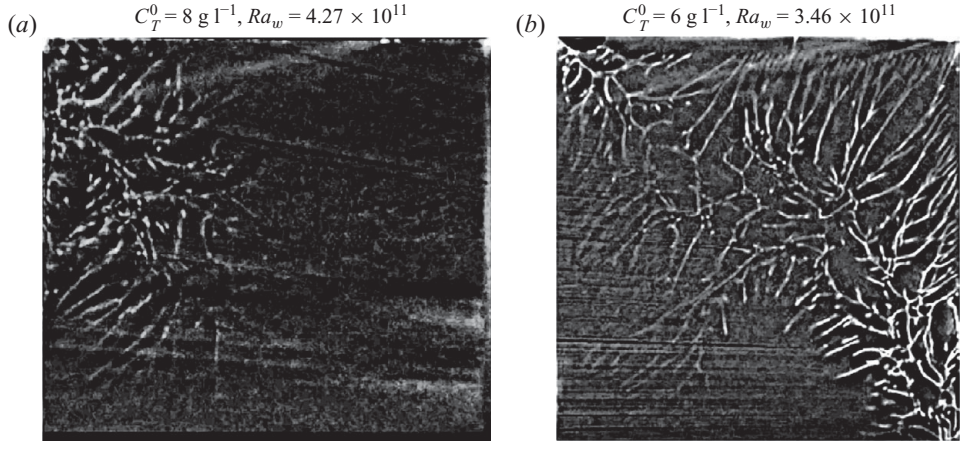

FIGURE 6. The plume structure evolution in the $Pe \sim 1$ regime: (*a*) the planform of plume structure at the start of the $Pe \sim 1$ regime and (*b*) the planform of the plume structure at the end of the $Pe \sim 1$ regime. The parameters corresponding to the images are shown in table 1.

The new phenomenon that is observed in our study is the presence of a regime between the advection and the combined regimes for $2.43 \times 10^{11} \leqslant Ra \leqslant 4.96 \times 10^{11}$, where $Sh \sim Ra$ approximately (figure 4*b*). The inset in figure 4(*a*) shows that in this new regime of convection $q \sim \Delta C^2$ in the corresponding $\Delta\rho/\rho$ range of $2.5 \times 10^{-3} \leqslant \Delta\rho/\rho \leqslant 5.1 \times 10^{-3}$, as against $q \sim \Delta C^3$ and $q \sim (\Delta C/2)^{4/3}$ respectively in the advection and the combined regimes. For reasons that will become obvious in § 4, we call this regime the $Pe \sim 1$ regime; we focus our attention on this regime further.

The identified scalings in each of the regimes need to be qualified by the fact that even though the total range of Rayleigh numbers in the present study is about two decades, the range of each of the regimes is not very large. In the present unsteady experiments, since the driving potential keeps decreasing, resulting in changing importance of advection and diffusion across the membrane, it may be unrealistic to expect large ranges of power-law scaling. The range of Ra of each of the regimes will depend upon the relation between the velocity of advection through the membrane and the ΔC across the membrane. A membrane with a smaller pore size will have a lower advection velocity through it, compared to that in a coarser membrane, for the same ΔC. This is because for the same large-scale flow strength that impinges on the membrane, the finer membrane needs a larger pressure drop across it to have the same advection velocity as the coarser membrane. The pressure drop across the membrane is determined by two properties of the membrane viz. its permeability κ and thickness l_m (see (5.2) in PA). The permeability is in turn a function of Γ and the wire diameter a of the membrane ($\kappa/a^2 = f(\Gamma)$, Graham & David 1986). The type of regime for a given Ra will hence depend on the permeability κ and l_m, as is also obvious from (4.18). Further investigations about the range of occurrence of each of the regimes as a function of Ra and membrane properties need to be conducted.

4. The $Pe \sim 1$ regime

The planform of plume structure at the beginning of the new regime, from the experiment with $C_T^0 = 8\,\mathrm{g\,l^{-1}}$ in figure 4(*a*), is shown in figure 6(*a*). As in PA, we

consider the large-scale flow as the flow in the bulk that causes a shear near the membrane and the flow through the membrane as through-flow (figure 8). It is known that the main effect of the large-scale flow is to align the sheet plumes near the membrane along the direction of the shear near the membrane (Theerthan & Arakeri 2000; PA). We expect the plume-free region in the planforms to be due to the impingement of the large-scale flow, driving a through-flow. As seen in figure 6(*a*), the alignment of plumes at the beginning of this new regime, even in the central region of the membrane, is less compared to that in the advection regime (refer figure 8*a* of PA). This lower alignment of plumes in the new regime implies a lower strength of the large-scale flow compared to that in the advection regime. Table 1 shows that the Reynolds number, $Re = W_* H/\nu$ of the large-scale flow corresponding to figure 6(*a*) is 824.5, less than $Re \sim 1200$ in the advection regime of PA, owing to the lower flux. We expect the impingement of this weaker large-scale flow on the membrane to result in a weaker through-flow than that in the advection regime. Figure 6(*b*) shows the planform towards the end of the new regime at $\Delta\rho/\rho = 3.73 \times 10^{-3}$. The planform shows only a small region that is free of plumes. Since the flux decreases as the experiment proceeds, the strength of the large-scale flow W_* (2.4) also decreases. We expect the lower strength of the large-scale flow to drive the boundary layers from a lower area on the impingement side to the other side. The plumes hence progressively cover more and more area on the surface of the membrane as the new regime progresses; the whole membrane area is covered by plumes at the end of the new regime.

The vacant region in the planforms of this regime indicates that there is a through-flow in the membrane and hence advective effects cannot be neglected in the membrane pore. Since the plume-free region decreases as convection proceeds from figures 6(*a*) to 6(*b*), we infer that the advection effects decrease from the beginning to the end of this new regime. If the transport through the membrane is purely by advection, we would observe the advection regime identified by PA with half the membrane surface area having plumes that are strongly aligned; such a regime is also seen at the beginning of our experiments. If pure diffusion occurred, the planform would be totally covered with plumes (PA05; PA). Hence, from the planforms of figure 6 and from the fact that the new regime occurs intermediate to the advection and diffusion regimes, we anticipate that both advection and diffusion play a non-negligible role in the transport inside the membrane pore in this new regime.

Assuming that the mechanism that determines the value of $\langle V_w \rangle$ in the advection regime, namely the impingement of the large-scale flow driving a flow that obeys the Darcy law, proposed in PA still holds in the new regime, we get

$$\langle V_w \rangle = f \frac{k}{2\nu l_m \Gamma} (g\beta q H)^{2/3}. \tag{4.1}$$

The prefactor f can be calculated as 1.64 by matching (4.1) with the expression for the through-flow in the advection regime,

$$\langle V_w \rangle = \frac{2q}{\Gamma \Delta C}. \tag{4.2}$$

The variation of Pe, calculated from (4.1) for the $C_T^0 = 10\,\mathrm{g\,l^{-1}}$ experiment in figure 4(*a*), is shown in figure 7. For the $\Delta\rho/\rho$ range of the new regime $2.5 \times 10^{-3} \leqslant \Delta\rho/\rho \leqslant 5.1 \times 10^{-3}$ ($2.43 \times 10^{11} \leqslant Ra \leqslant 4.96 \times 10^{11}$), Pe is of order 1; the advective and the diffusive effects are of the same order in the membrane pore in the new regime. We hence term this regime of convection as the $Pe \sim 1$ regime.

https://doi.org/10.1017/jfm.2011.142 Published online by Cambridge University Press

Figure	ΔC (g l^{-1})	$\Delta\rho/\rho$ ($\times 10^3$)	Ra ($\times 10^{-11}$)	ΔC_w (g l^{-1})	$(\Delta\rho/\rho)_w$ ($\times 10^3$)	Ra_w ($\times 10^{-11}$)	Flux (mg cm^{-2} min^{-1})	W_* (cm s^{-1})	Re ($=\frac{W_* H}{\nu}$)	V_i (μm s^{-1})	Image size (cm^2)
5(b)	5.11	3.60	3.64	2.55	1.80	1.82	0.072	0.27	724.5	4.6	15.2×14.0
6(a)	6.30	4.45	4.33	6.22	4.39	4.27	0.112	0.31	824.5	5.9	14.9×13.4
6(b)	5.29	3.73	3.77	4.85	3.42	3.46	0.077	0.28	740.8	4.8	14.9×14.2

TABLE 1. Parameters corresponding to the planforms of the plume structure.

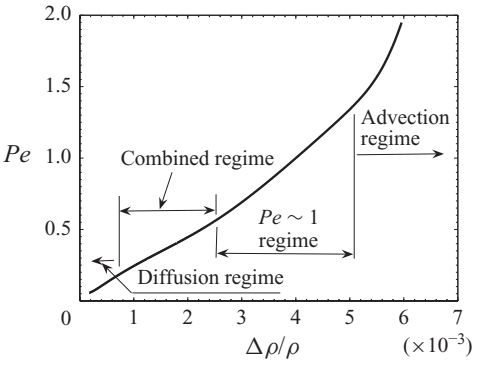

FIGURE 7. Variation of the membrane Péclet number (1.3) with the dimensionless density difference for the $C_T^0 = 10\,\mathrm{g\,l^{-1}}$ experiment in figure 4(*a*).

The $Pe \sim 1$ regime was observed in five experiments started with $C_T^0 = 10\,\mathrm{g\,l^{-1}}$, two experiments started with $8\,\mathrm{g\,l^{-1}}$, one experiment started with $C_T^0 = 15\,\mathrm{g\,l^{-1}}$ and one experiment started with $6\,\mathrm{g\,l^{-1}}$. Each of these experiments clearly showed a $Pe \sim 1$ regime wherein $Sh \sim Ra$ approximately. If we consider zero time as the time of the start of convection driven dynamics in an experiment, i.e. after the initial mixing, the new regime was observed between 60.23 and 513.37 min in the $C_T^0 = 10\,\mathrm{g\,l^{-1}}$ experiment (figure 3*a*). For the $C_T^0 = 8\,\mathrm{g\,l^{-1}}$ experiment shown in figures 4(*a*) and 5(*a*), the $Pe \sim 1$ regime occurred between 0 and 2005 min, while it occurred between 0 and 56 min in the $C_T^0 = 6\,\mathrm{gl^{-1}}$ experiment. The onset and the end of the new regime depend on the relative strengths of advection and diffusion inside the membrane. The relative strengths of these modes depend on Ra and the membrane properties. Hence, it is more appropriate to characterise the onset and the end of the regime in terms of an appropriate combination of Ra, κ and l_m than in terms of their temporal occurrence, since Ra itself is a function of time. The temporal occurrence of regimes will vary based on the membrane properties. The presence of a $Pe \sim 1$ regime shifts the occurrence of the combined and diffusion regimes to later periods of time compared to an experiment where the advection regime changes over directly to the combined regime as in PA. This is because the flux is lower in the $Pe \sim 1$ regime compared to that in the advection regime. The onset and the end of the regimes could however be expected to occur at the same value of some combination of Ra and the membrane properties; the appropriate combination of these independent variables is under investigation.

The exact range of Ra at which the $Pe \sim 1$ regime occurs seems to be slightly dependent on the perturbations due to the initial filling. There was a horizontal/vertical shift in q versus $\Delta\rho/\rho$ between experiments started with the same C_T^0, similar to that between the $C_T^0 = 10\,\mathrm{g\,l^{-1}}$ and $C_T^0 = 6\,\mathrm{g\,l^{-1}}$ experiments shown in figure 5(*a*). We expect this shift to be due to the change in initial conditions of filling, which could affect the strength of large-scale flow by changing the orientation of the sheet plumes between diagonal or parallel to walls. However, the flux scaling was independent of the initial perturbations, and as mentioned above, was observed in about nine experiments started at various concentrations. Due to this slight shift, we do not stress the range of Ra over which the regime occurs in the paper.

The range of Ra over which the $Pe \sim 1$ regime is obtained in the present experiments is limited by the underlying physical phenomena itself, viz. by the changing mode

of transport across the membrane from advection to diffusion. Using (4.1) and $Sh = C_1 Ra$, it can be easily shown that in the $Pe \sim 1$ regime,

$$Pe = \frac{C_1^{2/3} f}{2} \frac{\kappa}{\Gamma H^2} \left(\frac{Ra^4}{Sc} \right)^{1/3}. \tag{4.3}$$

If the regime exists only for $0.5 \leqslant Pe \leqslant 1.5$ (figure 7), (4.3) implies that the regime would exist only for

$$\xi \leqslant Ra \leqslant 3^{3/4}\xi, \quad \text{where } \xi = \frac{1}{\sqrt{C_1}} \left(\frac{\Gamma H^2}{f\kappa} \right)^{3/4} Sc^{1/4}. \tag{4.4}$$

Therefore, if the assumptions about the underlying physical phenomena are correct, the $Pe \sim 1$ regime is expected to exist only over a Rayleigh number range that varies by a factor of 2.28, similar to the range that we observe in our experiments. Equation (4.3) also shows that the values of Ra over which the $Pe \sim 1$ regime occurs will shift to larger values when a membrane with a larger value of Γ/κ is used and vice versa. These issues about the exact point of occurrence of each regime, and their range, needs further investigations with studies on membranes of varying properties, a task that is currently in progress. Since these issues are still not resolved, we do not stress the exact point of occurrence and the range of the $Pe \sim 1$ regime. Instead, since the study itself is the first one to detect such a regime, we focus further on the reason for such a regime and a phenomenology for the new flux scaling.

4.1. *Phenomenology of flux scaling in the $Pe \sim 1$ regime*

The planforms and the variation of Pe in the new regime show that advection and diffusion are equally important in this regime. This regime is a transition regime between the advection and diffusion regimes; the concentration drops across the membrane in these regimes being zero and a linear drop of $ql_m/\Gamma D$ respectively (see figures 1*a* and 1*b*). In the $Pe \sim 1$ regime, we expect a nonlinear concentration drop across the membrane, intermediate to that in the advection and diffusion regimes, with non-negligible concentration gradients at both the ends of the pore, as shown in figures 8(*a*) and 8(*c*). In this section, we solve the convection–diffusion equation in the membrane pore, with the unknown gradients on both sides of the membrane related by mass balance, to get an expression for the concentration drop across the membrane. The driving potential ΔC_n above and below the membrane in the no-impingement region is then obtained using this concentration drop. We find that $Ra_\delta^{-1/3}$, defined using the net flux and ΔC_n, remains a constant in the $Pe \sim 1$ regime; this finding helps us to obtain an expression for the dimensionless flux in this new regime.

Consider the control volumes of the top and the bottom tanks shown in figure 8(*b*). We denote the left half of the membrane as LH and the right half as RH, and consider the specific case of upward flow in LH and downward flow in RH. The phenomena are assumed to be symmetric with respect to a diagonal of the sum of the top and the bottom tank control volumes. The concentration values and profiles shown in figures 8(*a*) and 8(*c*) are area-averaged over LH and RH as the case might be. Let C_{L1} and C_{R1} be the concentration at $y = 0$ in LH and RH respectively while C_{L2} and C_{R2} be the concentration on the membrane surface at $y = l_m$ in LH and RH respectively. For the same $\langle V_w \rangle$ in LH and RH, symmetry implies

$$\left.\frac{\partial C}{\partial y}\right|_{LH,l_m} = \left.\frac{\partial C}{\partial y}\right|_{RH,0} = \xi_n \quad \text{and} \quad \left.\frac{\partial C}{\partial y}\right|_{LH,0} = \left.\frac{\partial C}{\partial y}\right|_{RH,l_m} = \xi_i, \tag{4.5}$$

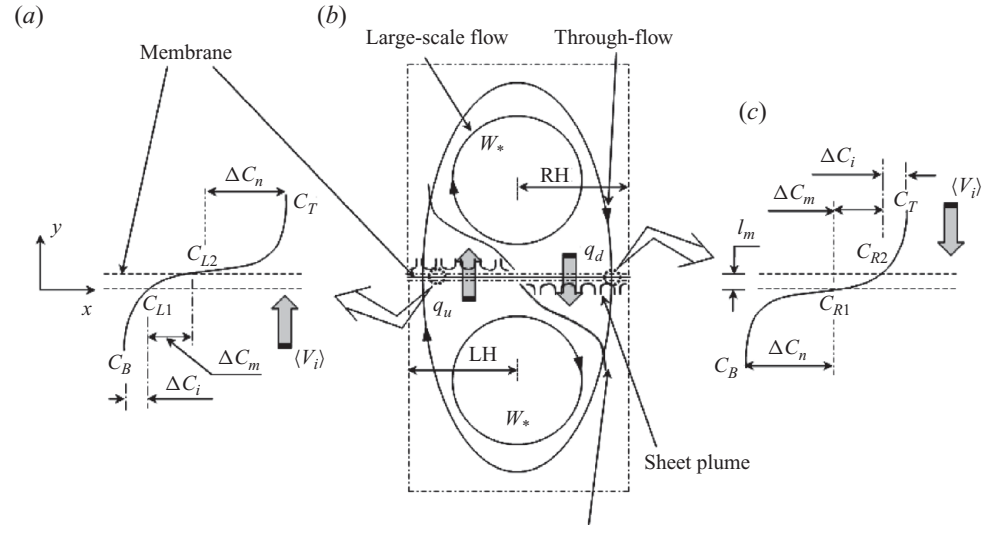

FIGURE 8. Schematic diagram of the flows and the inferred concentration profiles in the $Pe \sim 1$ regime: (a) the concentration profile on the left side of the membrane, (b) the control volume and the flows and (c) the concentration profile on the right side of the membrane.

where $C(y)$ is the concentration of NaCl in the membrane pore. The subscript i is used hereafter for the region of impingement of the large-scale flow and the subscript n for the region of no-impingement. The details of the basis for the division of the membrane surface into impingement and no-impingement regions are discussed in Appendix E.

The one-dimensional convection–diffusion equation with constant $\langle V_w \rangle$ inside the membrane pore is

$$\langle V_w \rangle \frac{\partial C}{\partial y} = D \frac{\partial^2 C}{\partial y^2}. \tag{4.6}$$

Here, we have used the quasi-steady approximation (§ 2.4) in using the steady form of the convection–diffusion equation. Solving (4.6) using (4.5) for LH, we get a condition to relate the concentration gradients on both sides of the membrane as

$$\xi_n = \xi_i \, \mathrm{e}^{Pe}. \tag{4.7}$$

From the mass balance in the top tank control volume, we get

$$\forall_T \frac{\partial C_T}{\partial t} = \Gamma C_{L2} \frac{A}{2} \langle V_w \rangle - \Gamma C_{R2} \frac{A}{2} \langle V_w \rangle - \Gamma \frac{A}{2} D(\xi_n + \xi_i), \tag{4.8}$$

where $\forall_T$ is the volume of the top tank and A is the cross-sectional area of the tank. From (4.7) and (4.8), the concentration gradient

$$\xi_n = \frac{\mathrm{e}^{Pe}}{1 + \mathrm{e}^{Pe}} \left(\frac{2q}{\Gamma \langle V_w \rangle} - \Delta C_l \right) \frac{\langle V_w \rangle}{D}, \tag{4.9}$$

with (4.7) then giving ξ_i where the lateral concentration difference $\Delta C_l = \Delta C_n - \Delta C_i$, with ΔC_n and ΔC_i being the concentration drops on the no-impingement and the impingement regions of the membrane (see figure 8). Solving (4.6) using (4.5), (4.7)

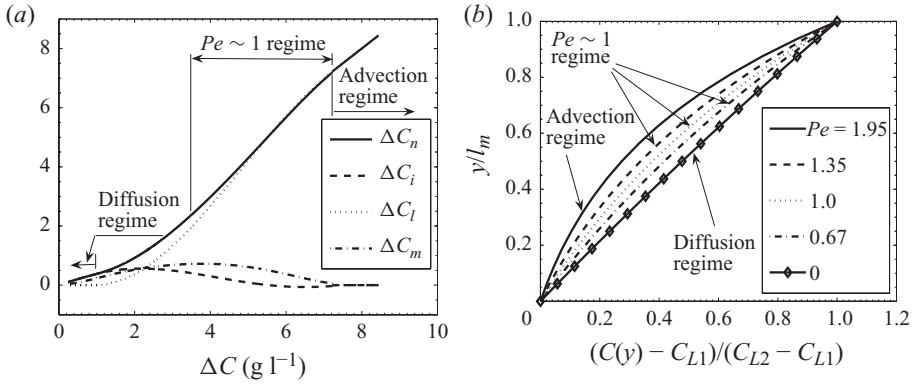

FIGURE 9. (*a*) Variation of ΔC_n (4.12), ΔC_i (4.13), ΔC_l (F 4) and ΔC_m (4.11) with ΔC. Curves in the advection and diffusion regimes are obtained from the expressions in the corresponding regimes. (*b*) Dimensionless concentration density inside the membrane pore in the different regimes.

and (4.9), $C(y)$ is obtained as

$$\frac{C(y) - C_{L1}}{2q/\Gamma\langle V_w\rangle - \Delta C_l} = \frac{e^{Pe_y} - 1}{e^{Pe} + 1}, \tag{4.10}$$

where $Pe_y = \langle V_w\rangle y/D$.

However, we still cannot calculate $C(y)$ from (4.10) as ΔC_l and C_{L1} are unknowns. Obtaining ΔC_l from (F 4), as shown in detail in Appendix F, the concentration drop across the membrane is obtained by substituting $y = l_m$ in (4.10) as

$$\Delta C_m = \frac{e^{Pe} - 1}{e^{Pe} + 1}\left(\frac{2q}{\Gamma\langle V_w\rangle} - \Delta C_l\right). \tag{4.11}$$

Note that (4.11) is the general expression for the concentration drop across a horizontal permeable membrane for all the regimes of convection due to unstable density gradients. In the advection regime, $2q/\Gamma\langle V_w\rangle = \Delta C$ (4.2) and $\Delta C_l \to \Delta C$ so that $\Delta C_m \to 0$ when $Pe \to 2ql_m/(D\Gamma\Delta C)$, in the diffusion regime, $\lim_{\langle V_w\rangle, \Delta C_l \to 0} \Delta C_m = ql_m/(\Gamma D)$, the same expression as obtained by PA05. Figure 9(*a*) shows the variation of ΔC_m for all the regimes of convection. Here ΔC_m increases from the beginning of the $Pe \sim 1$ regime to the end, showing the increasing effects of diffusion.

Using (4.11) and the condition $\Delta C_n + \Delta C_i + \Delta C_m = \Delta C$ obtained from figure 8, we get the relevant driving potentials in the no-impingement and the impingement regions respectively as

$$\Delta C_n = \frac{\Delta C}{2} + \frac{q}{\Gamma\langle V_w\rangle}\left(\frac{1 - e^{Pe}}{1 + e^{Pe}}\right) + \Delta C_l\left(\frac{e^{Pe}}{1 + e^{Pe}}\right) \tag{4.12}$$

and

$$\Delta C_i = \frac{\Delta C}{2} + \frac{q}{\Gamma\langle V_w\rangle}\left(\frac{1 - e^{Pe}}{1 + e^{Pe}}\right) - \Delta C_l\left(\frac{1}{1 + e^{Pe}}\right). \tag{4.13}$$

Figure 9(*a*) shows the variation of ΔC_n and ΔC_i in the $C_T^0 = 10\,\mathrm{g\,l^{-1}}$ experiment. In the advection regime, ΔC_n becomes ΔC and ΔC_i becomes zero, when $Pe \to 2ql_m/D\Gamma\Delta C$. At the beginning of the $Pe \sim 1$ regime, ΔC_i is negligible compared to ΔC_n. This clearly agrees with the observation from the planforms in figure 6(*a*) that the impingement

region is free of plumes. Note that ΔC_n decreases as the experiment proceeds and ΔC_n and ΔC_i become equal to $(\Delta C - \Delta C_m)/2$ as $\langle V_w \rangle \to 0$ in the diffusion regime. At this time, we expect the entire area of the membrane to be covered with plumes (PA05; PA). However, it appears that before the $Pe \sim 1$ reaches the diffusion regime, at some value of $\langle V_w \rangle$, the plume suction effects seem to become stronger than the impingement effects, resulting in zero drop in concentration across the membrane (figure 1*c*), giving rise to the combined regime. The above analysis is not valid in the combined regime that is observed here as well as in PA. The additional physical mechanisms, possibly plume suction, that cause no concentration drop in the membrane in the combined regime have not been considered in the above analysis.

In figure 9(*b*) we plot the concentration profile in the membrane in the different regimes, calculated using (4.10), (4.13) and (F 4) for the $C_T^0 = 10\,\mathrm{g\,l^{-1}}$ experiment in figure 4(*a*). The figure clearly shows the nonlinear concentration profile in the membrane pore in the $Pe \sim 1$ regime, illustrating that both advection and diffusion are important inside the membrane pore. With no advective effects in the diffusion regime, the profile becomes linear. The advection effects are expected to be important in the membrane pore when $Pe = 4$, as shown by PA in their figure 16(*a*). Since $Pe < 2$ in the present experiments, the concentration profile in figure 9(*b*) shows a substantial drop inside the membrane pore in the advection regime of the present study.

Now that we have obtained the relevant driving potentials for convection above and below the membrane (4.12) and (4.13), we try to relate the flux to these driving potentials, to arrive at a flux-scaling relation based on the above phenomenology. The flux given by (2.2) is a fictitious, uniform, downward flux on the surface of the membrane; in reality, half the membrane has downward flux q_d and the other half upward flux q_u (figure 8). Equation (2.2), along with (4.8) and (F 1), implies that the downward flux over RH,

$$q_d = \Gamma(C_{R2}\langle V_w \rangle + D\xi_i) \quad \text{at } y = l_m \quad \text{and} \quad q_d = \Gamma(C_{R1}\langle V_w \rangle + D\xi_n) \quad \text{at } y = 0. \tag{4.14}$$

Similarly, the upward flux over LH,

$$q_u = \Gamma(C_{L2}\langle V_w \rangle - D\xi_n) \quad \text{at } y = l_m, \quad \text{and} \quad q_u = \Gamma(C_{L1}\langle V_w \rangle + D\xi_i) \quad \text{at } y = 0. \tag{4.15}$$

Equations (4.14) and (4.15), along with (4.8), (F 1) and (2.2), imply that the net downward flux is

$$q_d - q_u = 2q; \tag{4.16}$$

downward flux is more than the upward flux, resulting in a decrease in concentration in the top tank.

If q_d and q_u are made dimensionless using $D\Delta C_i/Z_i$, where $Z_i = (\nu D/(g\beta\Delta C_i))^{1/3}$ is defined based on the concentration drop ΔC_i in the impingement region, we obtain the variation of the corresponding $Ra_\delta^{-1/3}$ as shown in inset (ii) of figure 10. $Ra_\delta^{-1/3}$ is not constant in the $Pe \sim 1$ regime and is much larger than 0.166, indicating the predominance of advection effects in the impingement region. Inset (i) of figure 10 shows the variation of $Ra_\delta^{-1/3}$ for q_d and q_u, calculated using the concentration drop ΔC_n and $Z_n = (\nu D/(g\beta\Delta C_n))^{1/3}$. This dimensionless flux is also not constant, indicating the presence of advective effects, but not as strong as on the impingement side as the values are close to the diffusion value of 0.166; diffusive flux is substantial on the no-impingement sides. The dimensionless downward flux is larger than the upward flux, the former being modestly more than 0.166 while the latter being less. Note that the difference between the curves in inset (i) of figure 10 is approximately

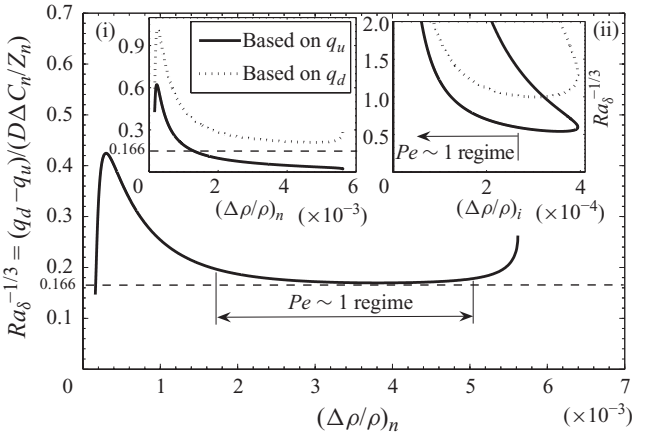

FIGURE 10. Variation of $Ra_\delta^{-1/3}$ (3.1) based on the concentration drop ΔC_n (4.12) on the no-impingement side for the difference between the downward flux q_d (4.14) and the upward flux q_u (4.15). Inset (i) shows $Ra_\delta^{-1/3}$ based on ΔC_n for q_d and q_u. Inset (ii) shows $Ra_\delta^{-1/3}$ based on ΔC_i (4.13) for q_d and q_u.

constant. This difference, in terms of $Ra_\delta^{-1/3}$ based on the net downward flux $q_d - q_u$ and ΔC_n, is shown as the main curve in figure 10. The dimensionless net flux, $(q_d - q_u)/(D\Delta C_n/Z_n)$, is a constant and has the value of 0.166, the same as that in the pure diffusive case, i.e.

$$q_d - q_u \sim \Delta C_n^{4/3}. \tag{4.17}$$

This behaviour seems to be the signature of the $Pe \sim 1$ regime of convection across a horizontal membrane due to unstable density gradients. Note that a constant dimensionless net flux does not imply that the boundary layers on the no-impingement side are same as that in pure RBC. As is clear from inset (i) of figure 10, q_d and q_u do not depend on ΔC_n in the same way as (4.17), only their difference does. Equations (4.16) and (4.17) imply that the flux q also scales as $\Delta C_n^{4/3}$, similar to that in the pure diffusion regime. However, since ΔC_n is a function of $\langle V_w \rangle$, the through-flow has an indirect effect on the flux scaling in this new regime.

Based on the above understanding, if we assume that $Ra_\delta^{-1/3} = E(\Delta C)$, where $Ra_\delta^{-1/3}$ is defined based on q and ΔC_n then using the expressions for ΔC_n from (4.12) and ΔC_l from (F 4) in the above equation, we get the flux scaling in the $Pe \sim 1$ regime as

$$\frac{2}{E^{3/4}}\left(\frac{Sh}{Ra^{1/3}}\right)^{3/4} - F_3\frac{4H}{f(\kappa/l_m)}\left(\frac{Sh\,Sc}{Ra^2}\right)^{1/3} - 2F_4\frac{Ra_l}{Ra} - 1 = 0, \tag{4.18}$$

where $F_3 = (1-e^{Pe})/(1+e^{Pe})$, $F_4 = e^{Pe}/(1+e^{Pe})$, Ra_l is the Rayleigh number based on ΔC_l and $E(\Delta C)$ is a function of ΔC, equal to 0.083 in the $Pe \sim 1$ regime (figure 10). Figure 4(*b*) shows that the solution of (4.18) matches well with the experimental data in the $Pe \sim 1$ regime. Equation (4.18) has the correct asymptotes. When $Pe \to 0$ in the diffusion regime, $F_3 \to 0$ and $Ra_l \to 0$, (4.18) then reduces to $Sh \sim Ra^{1/3}$. In the advection regime, $Ra_l \to Ra$, and as $E = Ra_\delta^{-1/3} = Sh/Ra^{1/3}$, (4.18) reduces to $Sh \sim Ra^2$. The general flux expression (4.18) could be used to predict the flux for a given membrane and Ra as long as the inertial effects are negligible in the membrane.

Equation (4.18) clearly shows that there is no single power-law scaling of Sh on Ra in the $Pe \sim 1$ regime. However, an equivalent, approximate single power-law

dependence of Sh on Ra in the regime, which is implied by (4.18), could be obtained as follows. If we substitute the linear approximation of $1+Pe$ for e^{Pe}, then $F_3 \sim -1$ and $F_4 \sim 1$. Since ΔC_l is linearly dependent on ΔC as shown in figure 9(a), Ra_l could be approximated as $A+BRa$, where $A=2.2\times10^{11}$ and $B=1.473$. Substituting these expressions in (4.18) and simplifying, we get

$$Sh \sim \left(\frac{2A+(2B+1)Ra}{c_2C_1^{5/12}Ra^{(5n+9)/12}+c_5Ra^{1/3}}\right)^3, \tag{4.19}$$

where we have substituted $Sh=C_1Ra^n$ for one of the Sherwood numbers in (4.18), $c_2=2/E^{3/4}$ and $c_5=4Hl_mSc^{1/3}/f\kappa$. Since $c_2C_1^{5/12} \ll c_5$ as $C_1 \sim 10^{-9}$ when $n \simeq 1$, we could neglect the first term of the denominator in (4.19), resulting in an approximate dependence of Sh on Ra given by

$$Sh \sim \frac{1}{c_5^3}\left(\frac{8A^3}{Ra}+12A^2(2B+1)+6A(2B+1)^2Ra+(2B+1)^3Ra^2\right). \tag{4.20}$$

The flux scaling is an outcome of the sum of various power laws in (4.20). If we try to find a single equivalent power law to (4.20), the first term in (4.20) will have negligible contribution to it at large Ra. The prefactor of the last term in (4.20) is of the order of 10^{-19}, while the prefactor of the term linear in Ra is of the order of 10^{-8}. The predominant single power-law dependence of Sh suggested by (4.20) is hence approximately $Sh \sim Ra$. Furthermore, to check that the $Sh \sim Ra$ scaling in the $Pe \sim 1$ regime is not an artefact of the small range of Ra, we substituted $Sh=C_1Ra^n$ in (4.18) and solved the resulting algebraic equation numerically to find n for the range of Ra in the $Pe \sim 1$ regime. Here n was equal to 1 in the $Pe \sim 1$ regime; the equivalent power law dependence of Sh on Ra given by (4.20) is definitely $Sh \sim Ra$ and is not an outcome of the short range of Ra.

4.2. *Plume spacings in the $Pe \sim 1$ regime*

The near-membrane sheet plumes in turbulent natural convection are the outcomes of the instability of the boundary layers feeding them (Sparrow & Husar 1969; Kerr 1996; Theerthan & Arakeri 2000; PA). Hence, measurement of the spacings between the plumes helps to indirectly infer the nature of the boundary layers. In the diffusion regime, averaging the Rotem & Classen (1969) similarity solution of laminar natural convection boundary layers over a mean plume spacing $\bar{\lambda}$, and matching the flux with that of Goldstein, Chiang & See (1990), PA05 found that for $Sc=600$,

$$\bar{\lambda} = 91.7Z_w, \tag{4.21}$$

where Z_w is defined by (2.5). Equation (4.21) implies the instability condition $Ra_\delta \sim 1000$. In the case of a weak through-flow, so that inertial effects are negligible in the boundary layers, PA found that the species boundary layers grow as (2.7). Using the instability condition $Gr_\delta \sim 1$, where $Gr_\delta = g\beta\Delta C_w\delta^3/\nu^2$ is the Grashoff number based on the species boundary-layer thickness and (2.5), they proposed that the mean spacing between the sheet plumes in the advection regime is

$$\bar{\lambda}_b = 2K^{2/3}Sc^{1/6}\sqrt{Z_{V_i}Z_w}, \tag{4.22}$$

with the prefactor $K=0.325$. These models matched observations, based on which Theerthan & Arakeri (1998), PA05 and PA hypothesised that the boundary layers in high-Rayleigh-number turbulent convection are laminar natural convection boundary layers. In both the advection and diffusion regimes, the probability density function

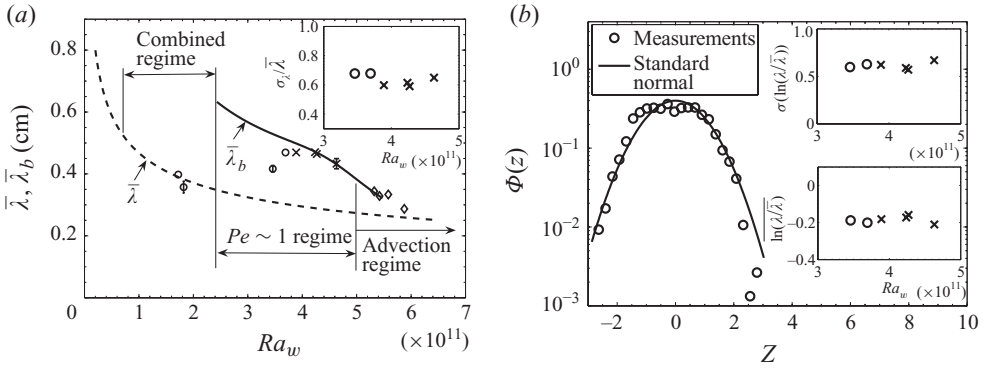

FIGURE 11. (*a*) Variation of the mean plume spacing with Ra_w in the different regimes of convection. Symbols: ◇, 10 g l^{-1} experiments; ×, 8 g l^{-1} experiments; ○, 6 g l^{-1} experiments. Inset shows the variation of dimensionless standard deviation of plume spacings with Ra_w. (*b*) Probability density function of $Z = (\ln(\lambda/\bar{\lambda}) - \overline{\ln(\lambda/\bar{\lambda})})/\sigma_{\ln(\lambda/\bar{\lambda})}$ in the $Pe \sim 1$ regime. Insets show the variation of the standardising variables $\sigma_{\ln(\lambda/\bar{\lambda})}$ and $\overline{\ln(\lambda/\bar{\lambda})}$ with Ra_w.

of plume spacings showed a common log-normal form (PA05; PA) and a common multifractal nature (Puthenveettil, Ananthakrishna & Arakeri 2005), independent of Ra.

In the $Pe \sim 1$ regime, the through-flow is very small to have only an indirect effect on the flux scaling; through-flow influences only ΔC_n, the flux scaling $q \sim \Delta C_n^{4/3}$ remains the same as that in the diffusion case. We now look at the effect of this very small through-flow on the mean plume spacing and the plume spacing density. The spacings between the plumes are measured perpendicular to the adjacent plumes in the planforms by capturing the coordinates of perpendicular lines to the adjacent plumes by mouse clicks. Measurements were made at a large number of locations in the planform to cover the complete range of spacings. The statistics of spacings are calculated from one experiment at $C_T^0 = 10\,\mathrm{g\,l^{-1}}$, two experiments at $C_T^0 = 8\,\mathrm{g\,l^{-1}}$ and one experiment at $C_T^0 = 6\,\mathrm{g\,l^{-1}}$. Different realisations of the plume spacings were obtained from each experiment by measuring the spacings in images that are separated by $t_m \sim 15$ s, which was larger than the average time of merging of the plumes $t_p \sim 10$ s. Since t_m is much smaller than the time scale of decrease of ΔC, $t_c = \Delta C/(\mathrm{d}\Delta C/\mathrm{d}t) \sim 444$ min at the beginning of the $Pe \sim 1$ regime, these images could be considered to be different independent realisations of the plume structure at the same Ra. In this way, by measuring from multiple images that are approximately at the same Ra_w, a minimum number of 500 measurements are used for the statistics at each Ra_w.

4.2.1. *Statistics of plume spacings*

Figure 11(*a*) shows the variation of the mean plume spacings with Ra_w over the duration of the present experiments. The effective Rayleigh number Ra_w is calculated based on the appropriate ΔC_w in each of the regimes; $\Delta C_w = \Delta C$, ΔC_n and $\Delta C/2$ respectively in the advection, $Pe \sim 1$ and the combined regimes. The error bars in the figure show the range of mean spacings obtained from different images at the same Ra_w. The mean plume spacings in the advection regime follow the expression (4.22) for $\overline{\lambda_b}$. The measurements at the beginning of the $Pe \sim 1$ regime, from planforms similar to those in figure 6(*a*) obtained from $C_T^0 = 8\,\mathrm{g\,l^{-1}}$ experiments, shown by crosses,

follow the $\overline{\lambda}_b$ curve, with spacings decreasing with the increase in Ra_w. The instability mechanism of the boundary layers in the advection regime seems to continue in the $Pe \sim 1$ regime. The circles marked in figure 11(*a*) are obtained towards the end of the $Pe \sim 1$ regime, from images similar to figure 6(*b*) obtained from a $C_T^0 = 6\,\mathrm{g\,l^{-1}}$ experiment. Note that the range marked as $Pe \sim 1$ regime in figure 11(*a*) is for the $C_T^0 = 10\,\mathrm{g\,l^{-1}}$ experiments, the transition to the combined regime takes place early for the $C_T^0 = 6\,\mathrm{g\,l^{-1}}$ experiment (see figure 5*a*). The mean spacings towards the end of the $Pe \sim 1$ regime deviate from the advection regime curve (4.22) and merge with the trend of plume spacings in the combined regime. This behaviour can also be noticed from the similarity of the plume structure in the planforms shown in figures 5(*b*) and 6(*b*). The gradual change in the plume structure from that in the advection regime (half–half division of plumes and plume-free areas along the diagonal; figure 8*a* of PA) to that in the combined regime (plumes covering the entire membrane surface; figure 5*b*) is also seen reflected in the mean plume spacing curve where the trend of mean plume spacings in the advection regime joins the trend in the combined regime through the $Pe \sim 1$ regime. We find the plume spacings to increase with Ra_w only at the end of the $Pe \sim 1$ regime. This increase occurs possibly due to the change in the nature of the instability of the boundary layers that occurs when the advective effects become appreciable.

The inset in figure 11(*a*) shows the standard deviation of the plume spacings, normalised with $\overline{\lambda}$ at each Ra_w, as a function of Ra_w in the $Pe \sim 1$ regime. Note that $\sigma_\lambda/\overline{\lambda}$ is approximately constant at 0.64; the variance is proportional to $\overline{\lambda}$. Since $\overline{\lambda}$ decreases with increase in Ra_w over most of the $Pe \sim 1$ regime, we could infer that the plumes become more closely and uniformly spaced with increase in Ra_w in this regime. The histograms of the plume spacings, normalised by their mean at different Ra_w in the $Pe \sim 1$ regime, were found to have the same long-tailed density as in PA and PA05 with a peak at $\lambda/\overline{\lambda} = 0.46$. Due to this common form of the histograms, we combine the logarithm of the normalised plume spacings from all the planforms in the $Pe \sim 1$ regime and plot the probability density function of the plume spacings in the standardised form, $Z = (\ln(\lambda/\overline{\lambda}) - \overline{\ln(\lambda/\overline{\lambda})})/\sigma_{\ln(\lambda/\overline{\lambda})}$, in figure 11(*b*). Here, a bar over a variable represents the mean and σ represents the standard deviation of the variable. The standard normal probability density function $\Phi = \mathrm{e}^{-Z^2/2}/\sqrt{2\pi}$ fits the data well. The insets in figure 11(*b*) show the variation of the standardising variables $\sigma_{\ln(\lambda/\overline{\lambda})}$ and $\overline{\ln(\lambda/\overline{\lambda})}$; these are constant at 0.6 and -0.18 respectively, similar to those in PA. This common log-normal density is similar to the observations of PA and PA05 in the advection and diffusion regimes. Even though the mean of the plume spacings is affected by the predominant mode of transport through the membrane, their density seems to be independent. As proposed by Puthenveettil *et al.* (2005), a common probability density function implies a common dynamics of generation of these planforms. Further quantitative investigations into this dynamics of initiation at a point, elongation and merger with the adjacent plume, elucidated in PA, PA05 and Puthenveettil *et al.* (2005), need to be conducted.

The plume-spacing statistics have implications for the development of predictive models for turbulent convection. The evolution of the mean plume spacing $\overline{\lambda}$ with Ra_w and the common probability density function of plume spacings could be used to construct wall functions for turbulent convection in the presence of a wall-normal flow. We could assume laminar natural convection boundary layers with a wall-normal flow to be present in between the sheet plumes that are separated by $\overline{\lambda}$. Averaging the temperature and velocity density obtained from analytical or numerical solutions of

such boundary layers over $\overline{\lambda}$, where $\overline{\lambda}$ is given by (4.21) or (4.22), could give the mean temperature and velocity profiles near the wall as a function of Ra_w. These wall functions could be used in turbulence modelling of convection with wall-normal advection.

5. Conclusions

The principal contribution of the present work is the discovery of a new regime of convection across a horizontal permeable membrane, driven by the unstable density difference due to a heavier layer of brine above the membrane and a lighter layer of water below it. In our experiments, where the concentration difference across the tanks keeps decreasing with time, thereby decreasing the Rayleigh numbers (figure 3*a*), and the flux, the new regime occurred after a regime similar to PA, wherein advection dominated in the membrane and the Sherwood number Sh scaled as Ra^2. The present experiments, by using a coarser and thicker membrane than PA, were able to extend the range of Ra at which the transition occurs from this advection regime to a regime where diffusion predominates the transport in the membrane. We find that in such a situation the transition region has two flux scalings; a new regime where Sh approximately scaled as Ra (figure 4*b*) occurred before the $Sh \sim (Ra/2)^{1/3}$ scaling, seen earlier in the combined regime detected by PA. A regime of convection where diffusion dominated the membrane transport, and $Sh \sim Ra_w^{1/3}$ similar to PA05, also occurred after the combined regime (inset in figure 5*a*).

The planforms of the plume structure in the new regime (figure 6*a*) showed less alignment of plumes than in the advection regime, due to a lower large-scale flow strength. The plume-free area decreased from approximately half at the beginning to almost zero at the end of this regime (figure 6*a,b*). Assuming that the mechanism of impingement of large-scale flow that occurs in the advection regime continues into this new regime, we estimated the membrane Péclet number (1.3) to be of order one. The new regime was hence termed as the $Pe \sim 1$ regime, characterised by a similar order of advection and diffusion in the membrane.

Using mass balance in both the tanks and symmetry assumptions, we obtained the concentration profile in the membrane (4.10), the concentration drop across the membrane (4.11) and the concentration drops in the fluid in the no-impingement ΔC_n (4.12) and the impingement regions (ΔC_i) (4.13) of the large-scale flow. The concentration profile was an exponential function of Pe_y, the Péclet number based on the vertical coordinate. The profile asymptotes to a linear concentration drop in the diffusion regime and to a zero concentration drop in the advection regime. The concentration profile, as well as the total concentration drop across the membrane, depended on the lateral concentration difference on the membrane. We find that in the $Pe \sim 1$ regime, the difference between the downward and the upward fluxes on the membrane, normalised by the diffusive flux in the no-impingement region, remains constant (figure 10) and is equal to the similar ratio in RBC. This behaviour appears to be a characteristic of the new regime. The flux in the $Pe \sim 1$ regime hence scales similar to that in RBC if the concentration drop in the no-impingement region is taken as the relevant driving potential (4.17). However, this does not imply that the boundary layers in the $Pe \sim 1$ regime are same as those in RBC, since the upward and downward dimensionless fluxes do not remain constant (inset (i) in figure 10), as they should, if the boundary layers were natural convection boundary layers. This change of the boundary-layer nature from that in RBC is also seen in the mean plume-spacing measurements in figure 11(*a*). The mean spacings follow the trend in the advection

regime; even the very small advection in the $Pe \sim 1$ regime seems to change the nature of instability of the boundary layers from that observed in RBC. We also observe that the probability density function of the plume spacings in the $Pe \sim 1$ regime follows a common log-normal form, similar to that observed in PA and PA05, implying a common generating mechanism of the plume structure mentioned in Puthenveettil *et al.* (2005).

We expect to have delineated all the possible regimes of convection below $Pe \sim 4$ due to the unstable density difference across a permeable membrane in the present study. However, various unknowns remain; the phenomenology of the combined regime observed in the present study as well as in PA remains a mystery. It appears that when the advection velocities reduce beyond a lower limit, some other physical mechanism, presumably plume suction, takes over and removes the concentration drop across the membrane. The exact physical reason for the dimensionless net flux in the $Pe \sim 1$ regime being a constant, shown in figure 10, also needs investigation. Furthermore, the present work has not investigated the dependence of the range of Ra of each regime on the membrane properties. Future efforts could try to obtain dimensionless combinations of Ra and membrane properties, to arrive at common criteria for the occurrence of each regime for membranes of different properties.

This research was conducted with the infrastructure set up under the FIST programme of the Department of Science and Technology. We wish to acknowledge the generous technical help of F. Lazarus in fabricating the experimental set-up.

Appendix A. Error due to the well-mixed assumption

The single-point measurement of concentration in the top tank C_T was assumed to represent the concentration of the entire top tank in (2.1) and (2.2). This assumption is justifiable if the top tank solution is well mixed, i.e. if $C_T = \langle C \rangle_{\forall_T}$, the volume-averaged value $(1/\forall_T) \int_{\forall_T} C \mathrm{d}\forall$. The bulk fluid is known to be well mixed in turbulent convection, which was also experimentally shown to be so for a similar set-up by Puthenveettil (2004) in their figure 2.9. However, the concentration in the boundary-layer region drops from the concentration in the bulk to that on the membrane surface. The error in assuming the measured C_T to be $\langle C \rangle_{\forall_T}$ will depend on the volume of the boundary-layer region with respect to the bulk region, i.e. on δ/H. If we make a reasonable assumption that there is a linear variation of concentration with height in the boundary layer of thickness δ, with the total concentration drop across δ being $\Delta C/2$, and the remaining bulk region being at C_T, it can be shown that

$$\langle C \rangle_{\forall_T} = C_T - \frac{\delta}{4H} \Delta C. \tag{A 1}$$

Since δ/H is of order 0.001, the error in neglecting the last term in (A 1) is negligible (0.025 % at $C_T = \Delta C = 10\,\mathrm{g\,l^{-1}}$ at the beginning of a $C_T^0 = 10\,\mathrm{g\,l^{-1}}$ experiment).

Appendix B. Proof of turbulence in the bulk in the present study

In turbulent convection, the turbulent vertical velocity fluctuations in the bulk $w' \sim W_*$ and the relevant length scale in the bulk is H (Adrian, Ferreira & Boberg 1986). The relevant dimensionless number that characterises the level of turbulence in convection is then the turbulent Reynolds number, $Re = W_* H/\nu$. From the definition of Sh and (2.4),

$$Re = (ShRaSc^{-2})^{1/3}. \tag{B 1}$$

Since it is known that the bulk becomes turbulent at $Ra \sim 10^5$ at $Pr = 6$ (Krishnamurti 1970), the bulk becomes turbulent at $Re \sim 30$. To arrive at this value, we have used the expression for Nu as a function of Ra and Sc suggested by Xia, Lam & Zhou (2002). Therefore, for the bulk to be turbulent in the present high-Sc experiments, Ra corresponding to $Re \sim 30$ is 2.6×10^8. The lowest Ra in the present experiments is $\sim 10^{10}$, so the bulk is fully turbulent in the present experiments.

It is well known that even though the mean temperature of the fluid layer increases with time, as long as the temperature difference across the fluid layer remains the same, the turbulence characteristics are not affected by the unsteadiness (Adrian *et al.* 1986). Such a situation occurs when the bottom surface of the fluid layer has a constant heat flux while the top surface is adiabatic/open to the atmosphere. In the present study, even though the mass flux at the bottom surface is unsteady, as we have shown in § 2.4, the unsteadiness of the flux is much slower than the unsteadiness of the large-scale flow and the near-membrane dynamics. Hence, the turbulence characteristics could be assumed to be the same as in the corresponding steady situation.

Appendix C. Exponential decay fit of C_T versus t

A decaying exponential curve is used to fit the C_T versus t data due to the following physical reason. Substituting ΔC from (4.2) in (2.1) and using (2.2) in the resulting expression, we get

$$C_T(t) = -B_1 \frac{\mathrm{d}C_T}{\mathrm{d}t} + B_2, \tag{C 1}$$

where $B_1 = H/\Gamma \langle V_w(t) \rangle$ and $B_2 = C_T^0/2$. For $\langle V_w \rangle$ constant with time, the solution to (C 1) is of the form

$$C_T(t) = B_2(1 + \mathrm{e}^{-t/B_1}). \tag{C 2}$$

Here B_1 becomes the time scale of concentration decrease. Since the theoretical concentration decay for a constant advection velocity is exponential, we use an exponential fit in the experiments.

In the present study, we use a sum of four decaying exponentials to fit the data, while PA and PA05 used a sum of three exponentials. A visually excellent fit was obtained with both the fits, as could be seen in figure 12(*a*). However, the r.m.s. error of the fourth-order and third-order fits were 0.0063 and 0.007 respectively; the fourth-order fit approximated the data better. Figure 12(*b*) shows that the residuals of the fourth-order fit were distributed randomly about zero, while those of the third-order fit showed a sinusoidal trend, indicating that the former approximates the trend of the data better. Even though both the fits captured the $Pe \sim 1$ and the advection regimes in the same way, the combined and diffusion regimes captured by the third-order fit deviated noticeably from that captured by the fourth-order fit. The inset in figure 12(*a*) shows that the third-order fit deviates noticeably towards the end of the diffusion regime. Each experiment was hence fitted with a fourth-order exponential curve and the corresponding fit coefficients were used in calculations for those experimental data alone. The fitted curve and its derivative were checked visually with the similar curves obtained from smoothed data points in each experiment. The derivative from the fit invariably passed through the mean of the derivatives obtained from the smoothed data points for all the experiments.

One can qualitatively understand the need for different exponential terms by looking at the equations that determine the C_T versus t evolution in the experiment. Equations (2.1) and (2.2) remain common to all the regimes, but the transport equations

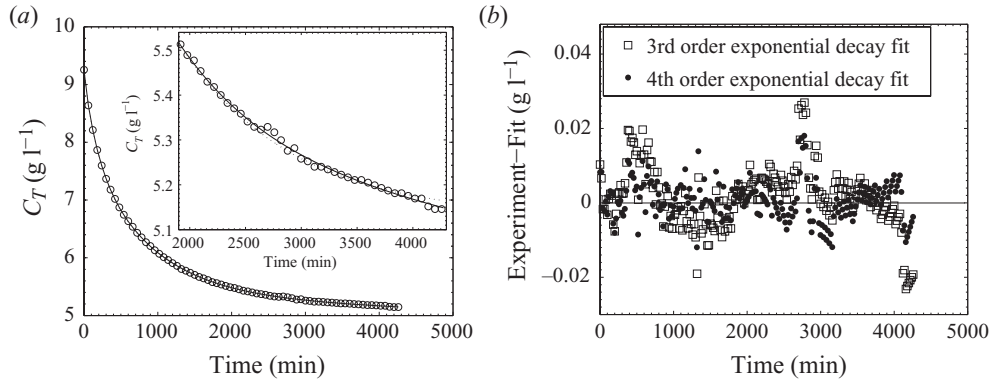

FIGURE 12. (*a*) Variation of C_T versus t corresponding to figure 4(*a*) along with the fourth-order and third-order exponential decay fits. The inset shows the zoomed view at the end of the diffusion regime. Symbols: ○, experimental data; —, fourth-order exponential decay fit; ..., third-order exponential decay fit. The experimental data are plotted at an interval of 60 min for clear visibility. (*b*) Residuals of the third-order and fourth-order fits for the data shown in figure 4(*a*).

across the membrane are different in different regimes. In the advection regime, the transport equations in the membrane are (4.1) and (4.2), while in the diffusion regime $q = D\Delta C_m/l_m$. In the $Pe \sim 1$ regime, the flux across the membrane is given by (4.14)–(4.16), while the equation is unknown in the combined regime. The fit constants d_n are such that $d_1 > d_2 > d_3 > d_4$; each of the exponential terms comes into play progressively with increasing time as the fit is of the form $\sum_n A_n \mathrm{e}^{-t/d_n}$. Since the transport equation across the membrane changes as the regime of convection shifts from one to another with increasing time, we expect the additional exponential decay terms to come into the picture successively with time. If there was only an advection regime, and with $\langle V_w \rangle$ constant, we would need only one exponential term (C 2) to fit the C_T versus t curve. However, this fit will not account for the change in transport equation across the membrane when the $Pe \sim 1$ regime is encountered, and the resulting change in trend of C_T versus t curve; an additional exponential decay term will be needed to account for this change in the trend. Similarly, additional exponential terms will be needed when other regimes are encountered so that the number of exponential terms needed is equal to the number of regimes in the experiment. The fit constants d_n then turn out to be the characteristic times in each regime.

Appendix D. Further estimates of near-membrane time scales

In the estimate of (2.6), the weight for ν and D is arbitrary, the scales are hence undetermined to a factor $\sqrt{Sc}$. A more rigorous estimate is obtained if we assume that the boundary layers between the sheet plumes are laminar natural convection boundary layers, the solutions of which are given by Rotem & Classen (1969). The species boundary-layer thickness δ_d as a function of the horizontal distance X for high-Pr fluids is given by (7.12) of PA05 as

$$\frac{\delta_d}{\bar{\lambda}} = \tilde{\eta}_{1\delta} Ra_\lambda^{-1/5} \left(\frac{X}{\lambda}\right)^{2/5}, \tag{D 1}$$

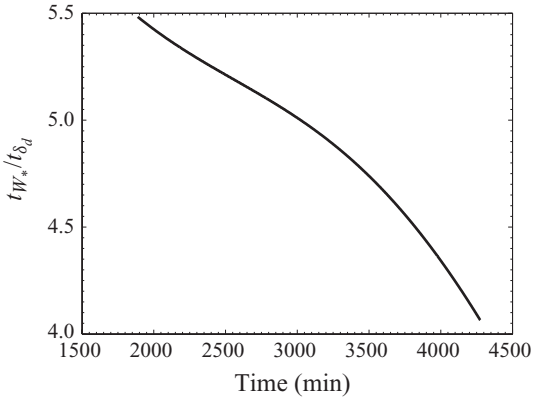

FIGURE 13. Variation of the ratio of the near-membrane time scale, t_{W*}/t_{δ_d}, with time in the diffusion regime.

where $\tilde{\eta}_{1\delta} = 3.5$ and $Ra_\lambda = g\beta\Delta C_w(\overline{\lambda})^3/\nu D$ is the Rayleigh number based on the mean plume spacing $\overline{\lambda}$. The characteristic velocity in these boundary layers is given by Rotem & Classen (1969) as

$$u_c \sim \frac{D}{L} Ra_L^{2/5}, \tag{D 2}$$

where L is the horizontal length scale, which could be taken as equal to half the mean plume spacing $\lambda_m/2$ (see Theerthan & Arakeri 1998; Puthenveettil & Arakeri 2005). In such a case, a time scale for the growth of the boundary layer is

$$t_{\delta_d} \sim \frac{\delta_d}{u_c}. \tag{D 3}$$

Using $Ra_L = Ra_\lambda/8$, $Ra_\lambda^{1/3} = 92$ (Puthenveettil & Arakeri 2005) and $X = \overline{\lambda}/2$ corresponding to the maximum boundary-layer thickness, (D 3) can be written as

$$t_{\delta_d} = 7.5\frac{Z_w^2}{D} = 7.5\, t_{U_w}\sqrt{Sc}. \tag{D 4}$$

Figure 13 shows that the variation of $t_{W*}/t_{\delta_d} \gg 1$, implying that the large-scale flow strength remains constant over the duration of the growth of the boundary layers; the quasi-steady assumption for the near-membrane boundary layers is valid.

Appendix E. Considerations behind division into impingement and no-impingement regions and neglecting the lateral flux

The fluxes in the analysis in § 4.1 are written at the membrane surface. On the membrane surface there is a clear demarcation of regions with sheet plumes and without sheet plumes. We expect the region without sheet plumes to be due to the impingement of the large-scale flow. Any impingement region on one surface of the membrane will have a no-impingement region below/above it on the other side. There is no lateral flux through the membrane due to the presence of the nylon wires. Hence, the flux that goes out of the top (bottom) tank through the impingement region has to be the same as the flux that comes into the bottom (top) tank through the no-impingement region. Hence, the impingement and the no-impingement fluxes are not decoupled in the analysis. However, the relative contributions of advection and diffusion to these fluxes change as the flow travels from the impingement region to the

no-impingement region through the membrane. The fluxes through the impingement and the no-impingement regions on the same surface of the membrane are also not assumed to be decoupled. This can be clearly seen from (4.16), where q_d is the downward flux through the impingement region and q_u is the upward flux through the no-impingement region on the same surface of the membrane.

In the analysis in § 4.1 we neglected the spatial variation of concentration along the membrane surface in the impingement and the no-impingement regions. The concentration on the membrane top surface was assumed to be uniform and equal to C_{R2} on the impingement side RH, while it was assumed to be uniform and equal to C_{L2} on the LH. This assumption is reasonable due to the following reasons. Since the bulk is well mixed, the impingement region of the large-scale flow, consisting of the fluid from the bulk, could be assumed to be of the same concentration. Since there is no lateral flux through the membrane, and since it is the fluid on the impingement side that comes out through the other side in the no-impingement region, the concentration on the no-impingement surface could also be assumed to be uniform.

The reasons for neglecting the cross-flux (lateral flux) within the membrane and on its surface are as follows. The Pe defined in the paper is based on the mean velocity through the membrane pores $\langle V_w \rangle$ and its thickness l_m; Pe is relevant only inside the membrane pore. Even though Pe is of order one, there is no cross-flux inside the membrane due to the presence of the nylon wires of the membrane. On the membrane surface in the impingement region, the advective flux will be normal since the lateral velocity component on the surface could be neglected due to the no-slip condition and the presence of vertical velocity in the membrane pores. There is no lateral diffusive flux on the impingement region on the membrane surface since the lateral concentration difference along the membrane surface could be neglected here, as shown above. Furthermore, the relevant velocity scale in the impingement region will be of the order of W_* and the relevant length scale H, as there are no boundary layers in this region. Note that $W_*/\langle V_w \rangle$ varies between 130.82 and 158.33 over the $Pe \sim 1$ regime so that the Péclet number calculated from W_* and H is $5.95 \times 10^5 > Pe_H > 3.79 \times 10^5$. Advective effects are hence predominant in the impingement region compared to the diffusive effects; even vertical diffusion can be hence neglected in the impingement region, and lateral diffusion will be even smaller.

In the no-impingement region, since there are boundary layers, diffusion is important. However, this diffusion will predominantly be in the vertical direction as the predominant concentration gradient is in the vertical direction. So here too the lateral diffusion can be neglected. At the line dividing the impingement and the no-impingement regions on the membrane surface, there is a lateral concentration difference $\Delta C_l = C_{R2} - C_{L2}$. However, the flux due to this difference along the membrane surface region is also negligible since the vertical thickness of the region over which this transport occurs is also negligible. Hence, cross-flux effects are negligible in the analysis of § 4.1.

Appendix F. Calculation of ΔC_l

Consider the control volumes of the top and bottom tanks as shown in figure 8. The mass balance of the bottom tank control volume can be written as

$$\forall_B \frac{\partial C_B}{\partial t} = \Gamma C_{R1} \frac{A}{2} \langle V_w \rangle - \Gamma C_{L1} \frac{A}{2} \langle V_w \rangle + \Gamma \frac{A}{2} D(\xi_n + \xi_i). \tag{F 1}$$

Using the conditions $q = -H_T \mathrm{d}C_T/\mathrm{d}t = H_B \mathrm{d}C_B/\mathrm{d}t$ and $\forall_T = \forall_B$, solving (4.8) and (F 1), we get $C_{R2} - C_{L2} = C_{R1} - C_{L1}$, implying that the concentration drop in the membrane ΔC_m is the same on LH and RH.

The lateral concentration difference on the membrane surface ΔC_l would be a function of the plume structure, large-scale flow strength and its orientation, the nature of which we are unable to determine as of now. However, we know the limits of ΔC_l; ΔC_l coincides with ΔC in the advection regime while it is zero in the diffusion regime because ΔC_n and ΔC_i are equal in the diffusion regime. We hence use a cubic interpolation between these limits to obtain ΔC_l. Here ΔC_l is approximated as

$$\Delta C_l = C_1 \Delta C^3 + C_2 \Delta C^2 + C_3 \Delta C + C_4, \tag{F 2}$$

where C_1 to C_4 have to be found by satisfying the following conditions:

$$\left.\begin{aligned} &\Delta C_l = \Delta C_{adv} \quad \text{for } \Delta C = \Delta C_{adv}, \\ &\Delta C_l = 0 \quad \text{for } \Delta C = \Delta C_{dif}, \\ &\frac{\mathrm{d}}{\mathrm{d}\Delta C}(\Delta C_l) = 0 \quad \text{for } \Delta C = \Delta C_{dif}, \\ &\frac{\mathrm{d}}{\mathrm{d}\Delta C}(\Delta C_l) = 1 \quad \text{for } \Delta C = \Delta C_{adv}. \end{aligned}\right\} \tag{F 3}$$

Here, $\Delta C_{adv} = 7.2\,\mathrm{g\,l^{-1}}$ is the concentration difference at which the advection regime changes to the $Pe \sim 1$ regime and $\Delta C_{dif} = 1\,\mathrm{g\,l^{-1}}$ is the concentration difference at which the diffusion regime begins, as calculated from the $10\,\mathrm{g\,l^{-1}}$ experiment in figure 4(a). Equation (F 2) along with (F 3) implies

$$\Delta C_l = \frac{(\Delta C - \Delta C_{dif})^2 (2\Delta C_{adv}^2 - \Delta C(\Delta C_{adv} + \Delta C_{dif}))}{(\Delta C_{adv} - \Delta C_{dif})^3}. \tag{F 4}$$

Figure 9(a) shows the variation of ΔC_l with ΔC for $\Delta C_{adv} = 7.2\,\mathrm{g\,l^{-1}}$ and $\Delta C_{dif} = 1\ \mathrm{g\ l^{-1}}$.

REFERENCES

Adrian, R. J., Ferreira, R. T. D. S. & Boberg, T. 1986 Turbulent thermal convection in wide horizontal fluid layers. *Exp. Fluids* **4**, 121–141.

Deardorff, J. W. 1970 Convective velocity and temperature scales for the unstable planetary boundary layer and for Rayleigh convection. *J. Atmos. Sci.* **27**, 1211–1213.

Dworecki, K., Slezak, A., Ornal-Wasik, B. & Wasik, S. 2005 Effect of hydrodynamic instabilities on solute transport in a membrane system. *J. Membr. Sci.* **263**, 94–100.

Goldstein, R. J., Chiang, H. D. & See, D. L. 1990 High Rayleigh number convection in a horizontal enclosure. *J. Fluid. Mech.* **213**, 111–126.

Graham, W. J. & David, F. J. 1986 The permeability of fibrous porous media. *Can. J. Chem. Engng* **64** (3), 364–374.

Kerr, R. M. 1996 Rayleigh number scaling in numerical convection. *J. Fluid. Mech.* **310**, 139–179.

Krishnamurti, R. 1970 On the transition to turbulent convection. *J. Fluid. Mech.* **42**, 295–307.

Lide, D. R. 2003 *CRC Handbook of Chemistry and Physics*, 84th edn., chap. 5. CRC.

Puthenveettil, B. A. 2004 Investigations on high Rayleigh number turbulent free convection. PhD thesis, Indian Institute of Science, Bangalore, http://etd.ncsi.iisc.ernet.in/handle/2005/140.

Puthenveettil, B. A., Ananthakrishna, G. & Arakeri, J. H. 2005 The multifractal nature of plume structure in high-Rayleigh-number convection. *J. Fluid. Mech.* **526**, 245–256.

Puthenveettil, B. A. & Arakeri, J. H. 2005 Plume structure in high-Rayleigh-number convection. *J. Fluid. Mech.* **542**, 217–249.

Puthenveettil, B. A. & Arakeri, J. H. 2008 Convection due to an unstable density gradient across a permeable membrane. *J. Fluid. Mech.* **609**, 139–170.

Radiometer Analytical SAS 2006 *Conductivity Theory and Practice Manual*. Radiometer Analytical.

Rama Reddy, G. V. 2009 Investigations on convection across a horizontal permeable membrane. Master's thesis, Department of Applied Mechanics, Indian Institute of Technology Madras, Chennai.

Rotem, Z. & Classen, L. 1969 Natural convection above unconfined horizontal surfaces. *J. Fluid. Mech.* **39** (1), 173–192.

Slezak, A., Dworecki, K. & Anderson, J. E. 1985 Gravitational effects on transmembrane flux: The Rayleigh–Taylor convective instability. *J. Membr. Sci.* **23**, 71–81.

Slezak, A., Grzegorczyn, S., Jasik-Slezak, J. & Michalska-Malecka, K. 2010 Natural convection as an asymmetrical factor of the transport through porous membrane. *Transp. Porous Med.,* **84** (3), 685–698.

Sparrow, E. & Husar, R. 1969 Longitudinal vortices in natural convection flow on inclined plates. *J. Fluid. Mech.* **37**, 251–255.

Theerthan, S. A. & Arakeri, J. H. 1994 Planform structure of turbulent Rayleigh–Bénard convection. *Intl Commun. Heat Mass Transfer* **21**, 561–572.

Theerthan, S. A. & Arakeri, J. H. 1998 A model for near wall dynamics in turbulent Rayleigh–Bénard convection. *J. Fluid. Mech.* **373**, 221–254.

Theerthan, S. A. & Arakeri, J. H. 2000 Planform structure and heat transfer in turbulent free convection over horizontal surfaces. *Phys. Fluids* **12**, 884–894.

Townsend, A. 1959 Temperature fluctuations over a heated horizontal surface. *J. Fluid. Mech.* **5**, 209–211.

Xia, K. Q., Lam, S. & Zhou, S. Q. 2002 Heat flux measurement in high-Prandtl-number turbulent Rayleigh–Bénard convection. *Phys. Rev. Lett.* **88** (6), 064501.